Article

Randomly Layered Superstructure of In_2O_3 Truncated Nano-Octahedra and High-Pressure Behavior

Shaojie Jiang,[†] Xiaobo Chen,[†] Xin Huang,[||] Can Li,[‡] Zhongwu Wang,[||] Bo Zhao,[⊥] Lihua Zhang,[▽] Guangwen Zhou,[†,#] Jiye Fang*,[†,‡]

[†]Materials Science and Engineering Program, State University of New York at Binghamton, Binghamton, New York 13902, United States.

[||]Cornell High Energy Synchrotron Source, Cornell University, Ithaca, New York 14853, United States.

[‡]Department of Chemistry, State University of New York at Binghamton, Binghamton, New York 13902, United States.

[⊥]College of Arts & Sciences Microscopy, Texas Tech University, Lubbock, Texas 79409, United States.

[▽]Center for Functional Nanomaterials, Brookhaven National Laboratory, Upton, New York 11973, United States.

[#]Department of Mechanical Engineering, State University of New York at Binghamton, Binghamton, New York 13902, United States.

Abstract

This study outlines the preparation and characterization of a unique superlattice composed of indium oxide (In_2O_3) vertex-truncated nano-octahedra, along with an exploration of its response to high-pressure conditions. Transmission electron microscopy and scanning transmission electron microscopy were employed to determine the average circumradius (15.2 nm) of these vertex-truncated building blocks and their planar superstructure. The resilience and response of the superlattice to pressure variations, peaking at 18.01 GPa, were examined by using synchrotron-based Wide-Angle X-ray Scattering (WAXS) and Small-Angle X-ray Scattering (SAXS) techniques. The WAXS data revealed no phase transitions, reinforcing the stability of the 2D superlattice comprised of random layers in alignment with a *p31m* planar symmetry as discerned by SAXS. Notably, the SAXS data also unveiled a pressure-induced, irreversible translation of octahedra and ligand interaction occurring within the random layer. Through our examination of these pressure-sensitive behaviors, we identified a distinctive translation model inherent to octahedra and observed modulation in the superlattice cell parameter induced by pressure. This research signifies a noteworthy advancement in deciphering the intricate behaviors of 2D superlattices under high pressure.

Keywords

Nano-octahedron, superlattice, high pressure, random layer, SAXS, planar symmetry

Introduction

Superlattices represent a distinct category of materials with periodic structures, potentially exhibiting unique properties such as dielectric,[1] optical,[1-4] magneto-optical,[5] electrical,[6] mechanical,[7] and gas sensing characteristics.[8] Within the realm of nanoscale self-assembly, the investigation of nano-polyhedron-based superlattices has been a subject of comprehensive research, both experimentally and theoretically, spanning several decades.[9-15] Prior research has predominantly centered on superlattices assembled using non-spherical building blocks,[16-17] such as nanocubes, which typically adopt simple cubic structures.[18-21] However, employing nano-octahedra as the assembly building blocks presents a compelling deviation.[14, 22] For instance, Zhu[23] et al. observed a fascinating monolayer arrangement comprising 70 nm gold nano-octahedra, while Gong[24] et al. confirmed the presence of simple hexagonal and monoclinic (reconstructed as triclinic in this work) superstructures of gold nano-octahedron self-assemblies *via* an SEM technique. Similarly, other research groups have also reported the existence of such simple hexagonal superstructures.[13] Moreover, novel *body-centered cubic* (*bcc*) superlattices, self-assembled with Pt_3Ni nano-octahedra, have been unveiled,[22, 25] thus introducing another unique arrangement to this family of packings. Notably, Minkowski proposed a widely recognized arrangement incorporating octahedral building blocks, which boasts the highest packing density of 18/19.[26] Interestingly, self-assembled superlattices adopting the Minkowski structure have been observed, regardless of the octahedron's compositions and sizes.[13, 24, 27-28]

Despite the presence of the aforementioned superlattice structures, which represent three-dimensional (3D) arrangements of building blocks and can be described using conventional unit cells, the reality of self-assembly involves building blocks with imperfect shapes and non-uniform sizes.[20] Additionally, various factors, including changes in concentration gradient during the assembling process, variation in assembling rate, and different environmental conditions such as temperature and humidity, further contribute to increasing the complexity of the self-assembly process. Consequently, self-assembled superlattices often exhibit abundant structure defects,[29-30] such as planar defects, which can significantly impact structure characteristics and may even mislead the structure evaluation if treated as a classic 3D periodic arrangement.

Among planar defects, stacking faults frequently appear in both natural and synthetic lamellar materials,[31] with instances observed in substances like coals,[32] graphene oxide,[33] vermiculite,[34] calcium silicate hydrates,[35] zeolite,[36] two-dimensional (2D) oxide colloids,[37] clay,[38] transition metal dichalcogenides such as WS_2 and MoS_2,[39] and chalcopyrite semiconductor nanosheets, notably $CuInS_2$.[40] These lamellar structures, characterized by stacking faults, present as irregularly accumulated layers, giving rise to XRD patterns that stand distinct from conventional crystalline materials. The inception of XRD analysis of layered structures dates back to Laue's discussion[41] in 1932, furthered by Warren's elaboration on the theory for XRD of random layer lattices.[42] Subsequent studies have vigorously sought to simulate and fit the XRD patterns of materials rich in stacking faults.[43-51] With stacking faults being a widespread phenomenon, our exploration of the self-assembled superlattice of indium oxide (In_2O_3) vertex-truncated nano-octahedra has revealed a superstructure defined by its randomly oriented, hexagonally close-packed octahedral layers. Using a high-pressure synchrotron X-ray diffraction technique,[52] we further identified an irreversible translation of the In_2O_3 octahedra within a randomly layered superlattice. To the best of our knowledge, no previous work has characterized such a superstructure derived from truncated nano-octahedra. Unveiling this random-layer superlattice not only expands the catalog of known self-assembled superlattice structures but also paves the way for innovative approaches in interpreting structural insights from Small-Angle X-ray Scattering (SAXS).[53] This has potential implications for applications such as optical and electronic functionalities.[54]

Experimental Section

In_2O_3 vertex-truncated nano-octahedra were synthesized using a hot organic solution in the presence of capping ligands and an oxidation agent, followed by self-assembly in a glass vial through slow solvent evaporation. A portion of the assembled superlattices was transferred into a gasket hole (200 microns in diameter) sandwiched between a pair of diamond anvils in a diamond anvil cell (DAC) for synchrotron-based Wide-Angle X-ray Scattering (WAXS) and SAXS determination. Meanwhile, another portion of the assembled superlattices was re-dispersed into hexane under ultrasonication, and the resulting suspensions were utilized for TEM characterization. More details regarding the synthesis, characterization, and structural analysis methods are provided in the Supporting Information.

Results and Discussion

Average Size of Building Blocks and 2D Superlattice

Fig. 1a presents the WAXS pattern of a superlattice composed of In_2O_3 vertex-truncated nano-octahedra (hereafter, truncated nano-octahedra), recorded at ambient pressure, which unveils the structure of these building blocks. All observed characteristic peaks align well with those from the standard In_2O_3 powder XRD (PXRD) pattern, as refined by Marezio[55] (Fig. 1b). This alignment confirms that the building blocks possess a pure In_2O_3 phase with a *bcc* structure (space group (206), $Ia\overline{3}$). A Rietveld refinement on the experimental WAXS pattern suggests a lattice parameter of $a' = 10.1412(3)$ Å, closely matching the unit cell size (10.118 Å or 10.14 Å) listed in the JCPDS cards (no. 06-0416 or no. 65-3170, respectively). Fig. 1c depicts a bright-field transmission electron microscopy (TEM) image of the In_2O_3 truncated nano-octahedra in various orientations, showcasing their morphology and size. Given that most of these octahedra have slightly truncated corners (as shown in Fig. 1d), determining their circumradius (r_c) *via* direct measurement from the center to a vertex is challenging. To evaluate the thickness of the assembly layer containing the In_2O_3 truncated nano-octahedra, the distance d_t between two parallel facets {111} in an octahedron was measured in the selected projection images, in which the imaged edge angle (109.92°) closely corresponds to the dihedral angle (109.47°) as illustrated in Fig. 1e. Consequently, the circumradius can be expressed as $r_c = d_t \sqrt{3}/2$ (see Fig. S1 for details). By measuring d_t of more than ~25 truncated nano-octahedra with the same orientations (Fig. S2), the average value was determined as $17.5\underline{8}$ nm, resulting in an average circumradius r_c of $15.2\underline{2}$ nm.

Fig. 2a displays a secondary electron (SE) image taken using a nanometer probe in an aberration-corrected scanning TEM (STEM), showing the self-assembled superlattice composed of the In_2O_3 truncated nano-octahedra. This image reveals that on a 2D plane, the octahedral building blocks align themselves in straight lines with consistent orientations, thereby forming well-ordered layers. Based on these observations (refer to the zoomed-in image in Fig. 2b), we propose a structure model that features a hexagonally close-packed lattice (Fig. 2c). Similar to the 2D hexagonal close-packing of spheres, in planarily packed building blocks, each truncated nano-octahedron is surrounded by six neighboring octahedra of the same orientation, leading to a coordination number of six. The unit cell (Fig. 2d) for this octahedron-containing layer adopts a lozenge shape with an obtuse angle of 120°, which aligns with the wallpaper group *p31m* symmetry. The red triangles depicted in Fig. 2d represent a class of the 3-fold rotation axes that do not lie on the mirror planes (dark lines), thereby confirming the planar *p31m* symmetry rather than *p3m1*. For any two contiguous octahedra in a layer, the vertex of one octahedron is positioned at the edge center of the other, with their adjacent facets parallel to each other. For every three contiguous building blocks – assume they are perfect octahedra, two tetrahedral voids with a shared common vertex form at the center region, resulting in a packing fraction of 8/9 (refer to Fig. S3). This specific 2D hexagonally close-packing has also been observed for gold and silver octahedra.[23, 56] As for all octahedra within a layer, their top and bottom facets establish two planes parallel to the layer, suggesting the potential for stacking these layers on top of one another (Fig. 2a). Such stacking of layers has been confirmed to yield either a simple hexagonal superlattice[13, 24] or a monoclinic superlattice,[24] which we confirmed as triclinic. In addition to the electron microscopic observations (Fig. 2a,b), further evidence supporting the assigned wallpaper group *p31m* symmetry of the close-packed layers can be gleaned from the agreement between the diffraction peak positions in their SAXS pattern and those calculated using a planar *p31m* lattice, as depicted in Fig. 3b,d and Table 1 (*vide infra*).

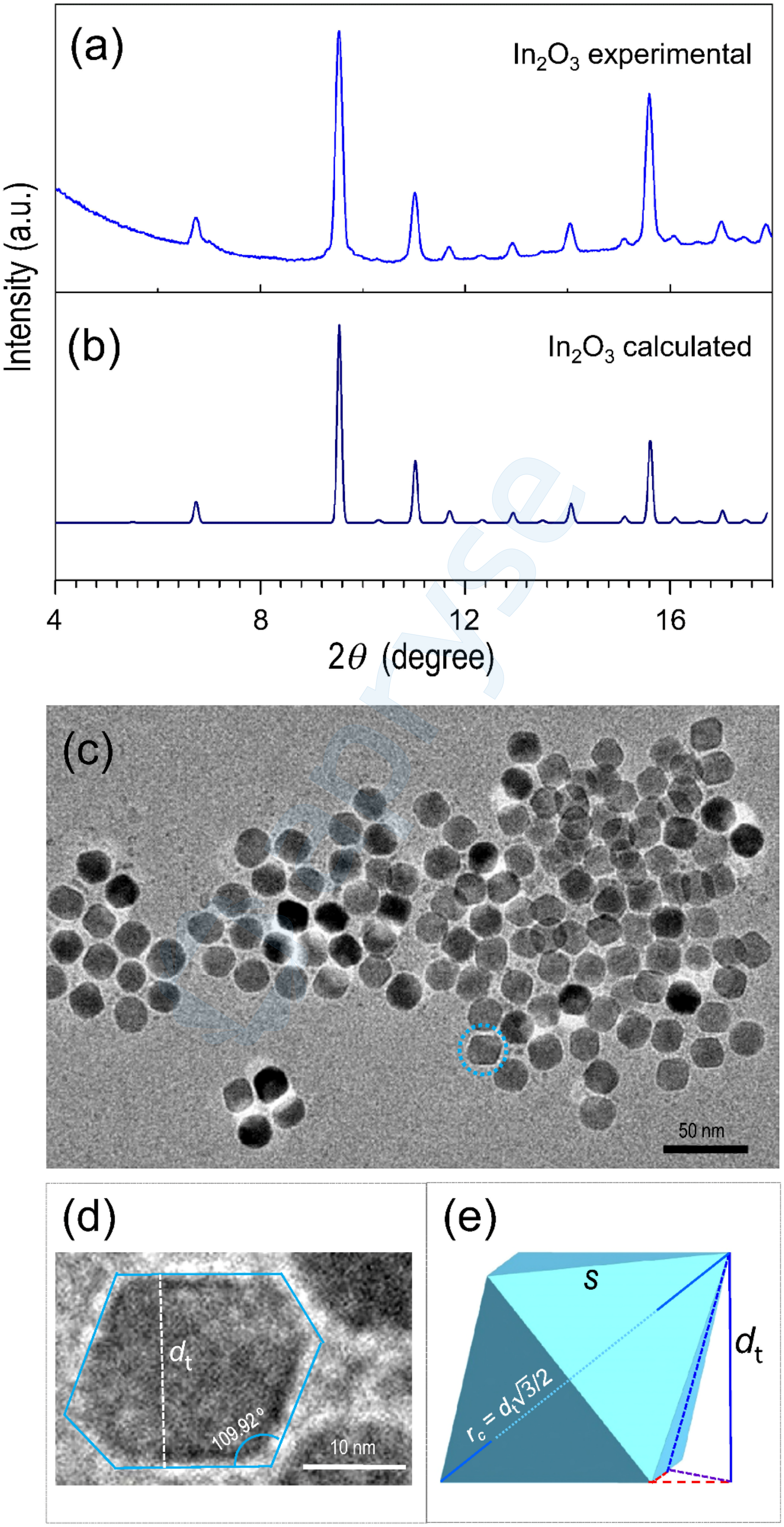
(a)
In$_2$O$_3$ experimental
Intensity (a.u.)
(b)
In$_2$O$_3$ calculated
4
8
12
16
2θ (degree)
(c)
50 nm
(d)
d_t
109.92°
10 nm
(e)
s
d_t
$r_c = d_t\sqrt{3}/2$

Fig. 1. Indium oxide (In_2O_3) truncated nano-octahedra. (a), WAXS pattern of the In_2O_3 superlattice; (b), calculated In_2O_3 PXRD pattern; (c), typical bright-field TEM image of In_2O_3 truncated nano-octahedra; (d), zoomed-in view of an In_2O_3 truncated nano-octahedron marked by the blue dotted circle in (c); and (e), structure model of an octahedron, showing $r_{\mathrm{c}} = d_t \sqrt{3}\,/2$ (s is a side-length of the nano-octahedron, $s = \sqrt{2}\, r_{\mathrm{c}}$).

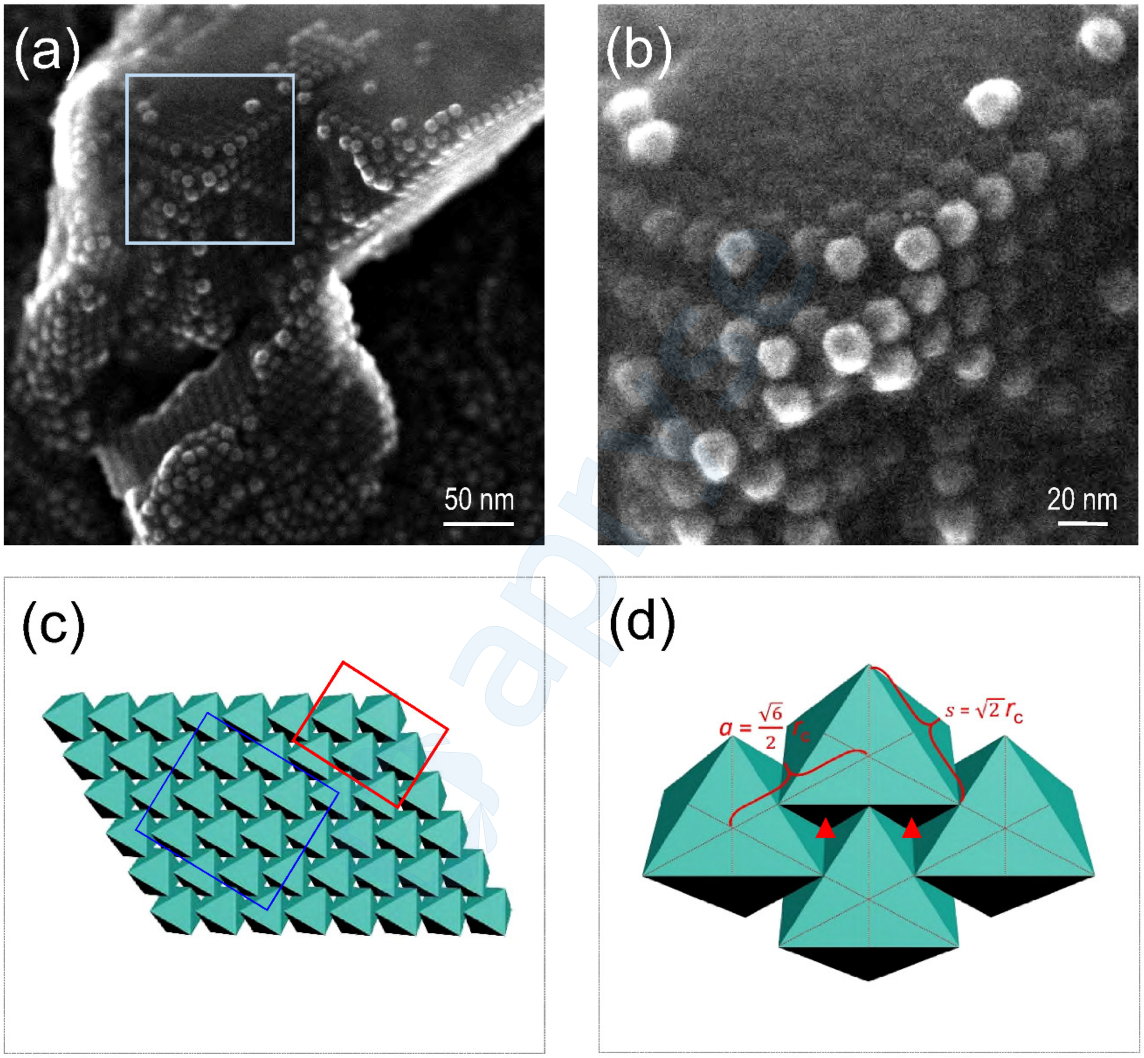

Fig. 2. Indium oxide planar superlattice. (a), SE image obtained by the STEM; (b), zoomed-in view of the area marked by the blue box in (a); (c), structure model of a hexagonally close-packed octahedral layer (the red box is a selected area for a zoomed-in view of the unit cell, whereas the blue box is a selected area for packing fraction calculation shown in Fig. S3); (d), unit cell of the 2D close-packed hexagonal lattice superstructure with wallpaper group *p31m* symmetry. Note that the red triangles represent a class of the 3-fold rotation axes that do not pass through the mirror planes (dark lines), and the actual truncation on vertices wouldn't affect the packing symmetry in this model.

Considering that the SE image provides local superstructure details rather than overarching packing information, we utilized synchrotron SAXS to investigate the superlattice structure. Fig. 3a,b presents the 2D X-ray diffraction pattern and its corresponding intensity-integrated one-dimensional (1D) pattern, respectively. The diffraction patterns exhibit five peaks/rings, including a notably faint one (marked in the inset of Fig. 3b) that has a *d*-spacing of 7.3 nm. The first and second strong rings (Fig. 3a) or sharp peaks (Fig. 3b) imply a high degree of crystallinity in the superlattice. The spotty diffraction rings in Fig. 3a indicate that the superlattice contains large crystallites with non-uniform orientations. It's worth mentioning that the intensities of Bragg peaks (20) and (21) in Fig. 3b appear notably weaker compared to the first two peaks. This decline in intensity is consistent with the exponential decrease in X-ray scattering intensity at a small angle range as a function of scattering vector (q) or two Theta (2θ), which can be estimated or evaluated using the Guinier Approximation.[57-58] Such a rapid change in intensity is commonly observed in SAXS for powder assembly samples.[52, 59] The prominence on the left of the first peak in Fig. 3b, rather than a diffraction peak, denotes the high-intensity central area resulting from the beam stop's deviation, as depicted in Fig. 3a. If considered a diffraction peak, this prominence would suggest a *d*-spacing of approximately 21 nm, implying the existence of a diffraction ring with a *d*-spacing of around 21 nm, which, however, is not observed in the 2D pattern. Efforts to index peaks in the search of potential unit cells yielded no structure that aligns with the experimental pattern. To decipher the superstructure, we simulated SAXS patterns of several reported self-assembled octahedron superstructures, including simple hexagonal,[24] triclinic,[24] and *bcc*[25] superlattices, for comparison with the experimental pattern (Fig. S4a-c). When constructing the unit cells of the reported superlattices, we positioned the coordinates of the octahedra at the octahedral geometric center. Fig. S4d-f depicts the unit cells, space groups, and derived cell parameters of the corresponding superlattices that we proposed, respectively. As presented in Fig. S4d-f, we calculated the sizes of these simulated superlattices using our experimental measurements of the In_2O_3 truncated nano-octahedra as the building blocks (*i.e.*, $r_c = 15.2\underline{2}$ nm). Upon comparing the experimental patterns, none of the reported structures matched. The fact that the number of diffraction peaks in the simulations significantly exceeds that in the experimental pattern suggests that the In_2O_3 superlattice possesses a high-symmetry structure and fewer diffraction planes.

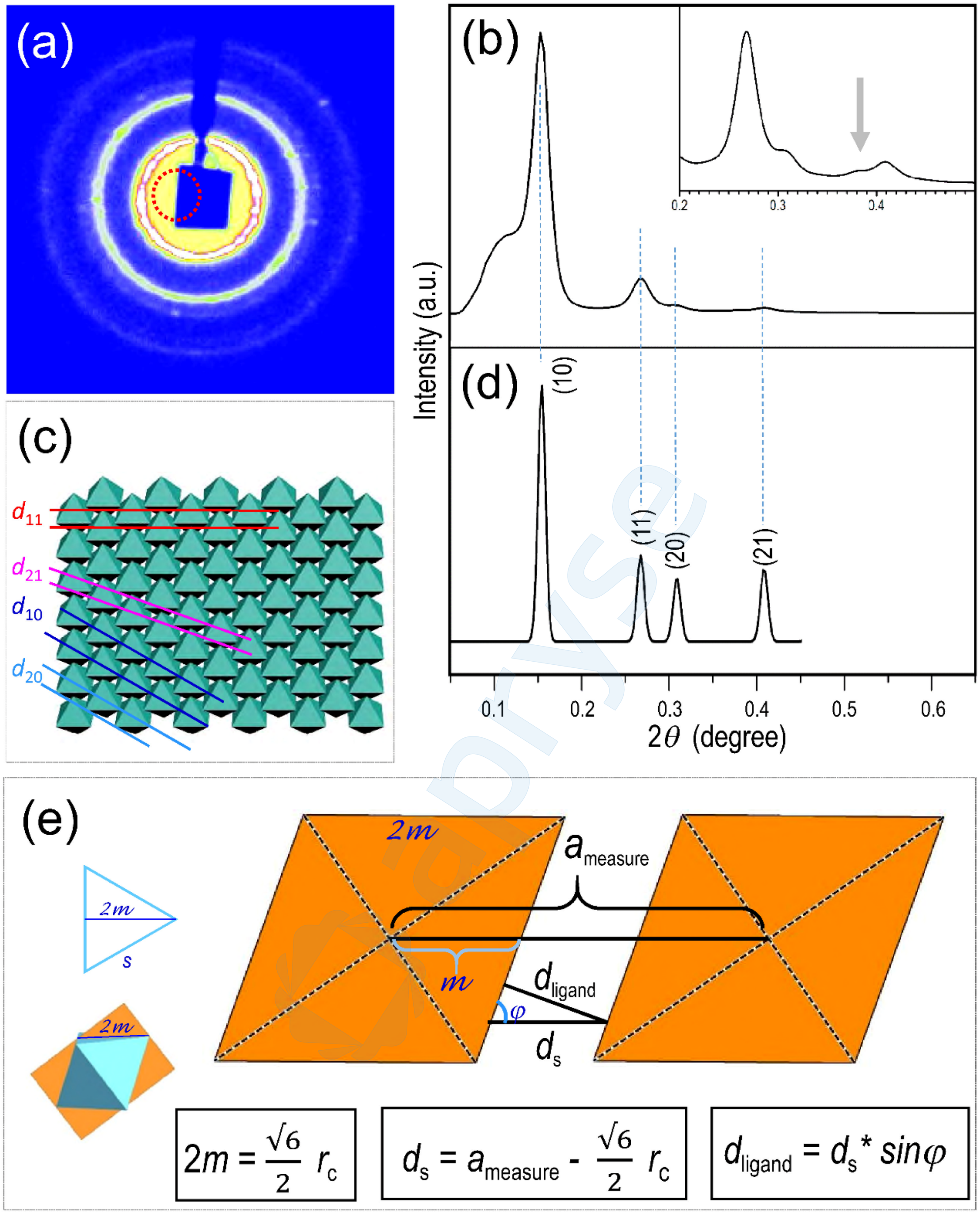

Fig. 3. Diffraction patterns and structure model of superlattices consisting of In_2O_3 truncated nano-octahedra. (a), typical 2D SAXS pattern; (b), corresponding intensity-integrated 1D pattern. The inset is a zoom-in 1D pattern, showing the weakest reflection peak; (c), proposed 2D hexagonal close-packed pattern with a plane symmetry group *p31m* and its in-plane reflection lattice lines; (d), calculated SAXS peaks according to this 2D hexagonal lattice with wallpaper group *p31m*; (e) illustration of a cross-section of the packed building blocks, showing their separation distance, in which, $2m = \ell \sin 60^\circ = (\sqrt{2}\, r_c)\, \sqrt{3}/2 = \frac{\sqrt{6}}{2} r_c$; $d_s = a_{measure} - 2m = a_{measure} - \frac{\sqrt{6}}{2} r_c$; $d_{ligand} = d_s * \sin\varphi = \frac{2\sqrt{2}}{3} d_s$ (refer to Fig. S1).

Given the observation that the superlattice presents only five observable diffraction planes, it is plausible that the actual lattice is comprised of monolayers with various sizes and orientations, negating the presence of a conventional 3D unit cell. Warren[42] expounded the diffraction rules of lattice structures within such random layers. In scenarios where the layers are parallel, equidistant, and arbitrary in translations and rotations, the usual reflections (*hkl*) vanish, given the lack of ordered building block arrangements between layers to form (*hkl*) planes, thereby preventing conditions for constructive interferences. Instead, the diffraction pattern comprises two types of peaks: out-of-plane reflections (*00l*), stemming from the stacked layers, and in-plane reflections (*hk*) that originate from the layers themselves.[42] It's notable that the (*00l*) reflections fail to exist when the layers are neither parallel nor equidistant, or when there are insufficient layers to stack up and generate detectable constructive reflections. The superlattice, comprising hexagonal lattice layers, is capable of generating the first four in-plane reflections (Fig. 3c), (*10*), (*11*), (*20*) and (*21*), irrespective of the layer stacking. The wallpaper group *p31m* symmetry of this assembly results in identical cell parameters $a = c$, thereby causing an overlap of the (*hk*) and (*kh*) reflections. We chose the *d*-spacing of the (*11*) reflection to calculate the parameter for two reasons: 1) the (*10*) reflection might merge with (001) reflection, potentially leading to an inaccurate value for parameter calculation; 2) the (*20*) and (*21*) reflections are too weak to accurately determine their *d*-spacings. Consequently, we calculated the superlattice unit cell parameter a as $a = 2 * d_{(11)}$. According to this superstructure model, Table 1 provides a comparison of *d*-spacing between the experimental determinations and the calculated values. Fig. 3d showcases the calculated peaks in the in-plane diffraction pattern, which aligns well with the experimental SAXS peaks, excluding the weakest one at ~7.3 nm (Fig. 3b). This faint reflection could arise from slight positional deviations of the octahedra within certain layers. Having obtained the superlattice parameter $a_{measure}$ from SAXS and the average size of the truncated nano-octahedra from TEM, we calculated the separation between two facets of two neighboring octahedra as $d_s = a_{measure} - \frac{\sqrt{6}}{2} r_c = (10.4\underline{1} * 2) - \frac{\sqrt{6}}{2} * 15.2\underline{2} = 2.1\underline{8}$ (nm) (Fig. 3e). Accordingly, the length of the uncharged organic ligands[60] (oleic acid and oleylamine) that join the 2D superlattice should be $d_{\text{ligand}} = d_s * \sin\varphi = \frac{2\sqrt{2}}{3} d_s = 2.0\underline{5}$ (nm) (refer to Fig. 3e and Fig. S1), suggesting that the ligands interpenetrate each other to stabilize the connected octahedra, given that the length of the ligand is around 2.0 nm or less (*vide infra*).[61] Another question arising from the randomly layered superlattice pertains to the existence of out-of-plane (*00l*) reflections. Given the thickness of the octahedron layer d_t (17.5$\underline{8}$ nm) (Fig. 1b) and the ligand length $d_{\text{ligand}} = 2.0\underline{5}$ nm, the theoretical *d*-spacing for (*001*) reflection would be $d_{001} = d_t + d_{\text{ligand}} = 19.6\underline{3}$ nm. However, no traces of any diffraction ring in the area where the *d*-spacing is around 19.6 nm are observed. This suggests that the close-packed octahedral layers do not stack in a parallel or equidistant manner, even though Fig. 2a depicts the local features of parallel layers.

Table 1. *d*-Spacing values of 2D hexagonal superlattice containing truncated nano-octahedra

	Experimental *d* (nm)	Calculated *d* (nm)
d_{10}	18.2226	18.0294
d_{11}	10.4093	10.4093
d_{20}	9.0967	9.0147
d_{21}	6.8106	6.8145

2D Superlattice Unit Cell as a Function of Pressure

To gain further insights into the behavior of In_2O_3 truncated nano-octahedra under pressure, we conducted high-pressure synchrotron XRD measurements, capturing both SAXS and WAXS data, up to a pressure of 18.01 GPa. Previous studies have suggested pressure-induced phase transition onsets for In_2O_3 at 35.1 GPa[62] and 23.58 GPa[63] for bulk and nano-phase, respectively. As shown in Fig. S5, our refinement of the WAXS patterns revealed no phase transition throughout the entire compression and decompression processes, as our maximum applied pressure remained lower than the reported phase transition pressures. As the pressure increased from ambient to 8.43 GPa, the lattice parameter a' for the In_2O_3 atomic structure consistently decreased from 10.1412(2) Å to 10.0565(6) Å. When the pressure was further increased continuously up to 11.62 GPa, the a' slightly rose to 10.0911(6) Å. Further compression up to 18.01 GPa resulted in a reduction of a' down to 10.0592(7) Å. Upon release of pressure, a' followed a general trend of increase and eventually reverted to a value close to its initial measurement, indicating the reversibility of the compression process.

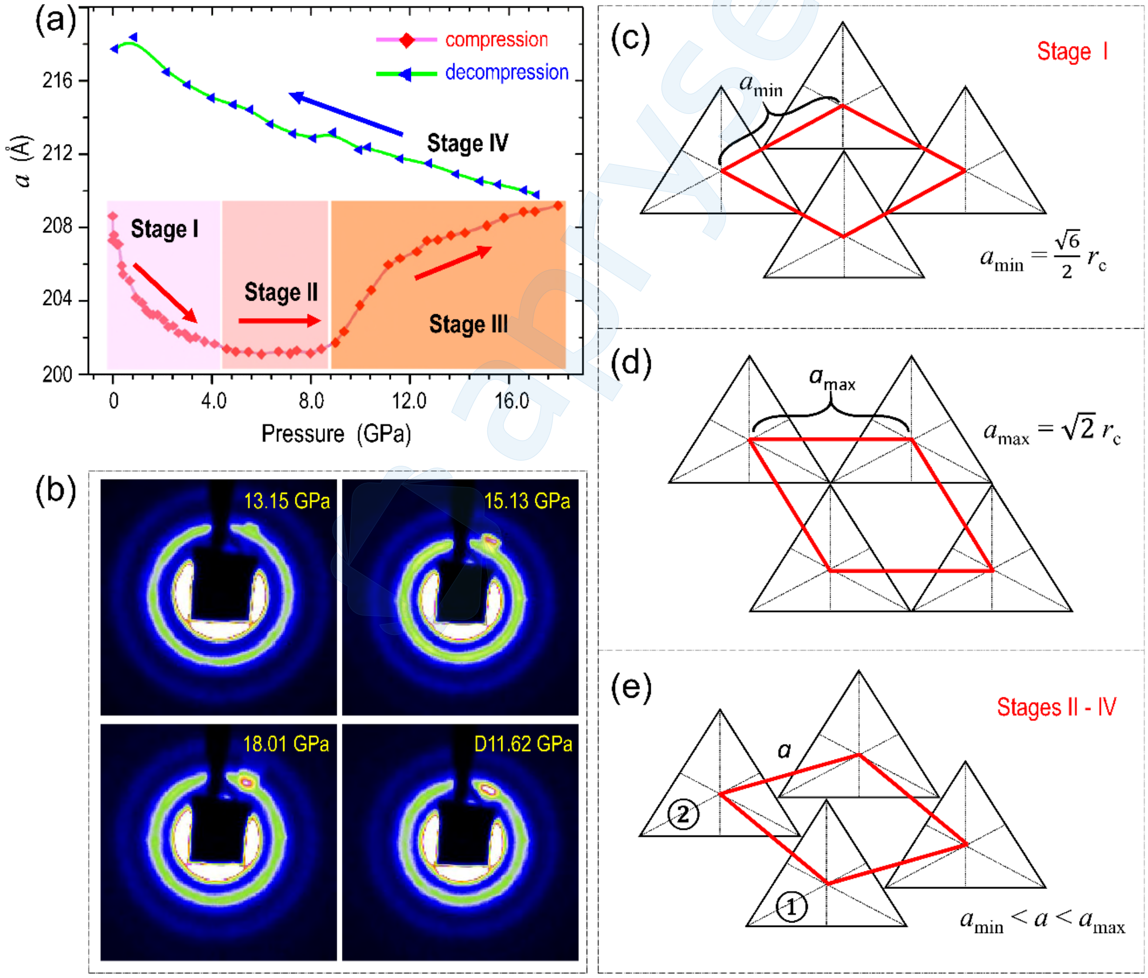

Fig. 4. Indium oxide superlattice under pressure. (a), variation of superlattice cell parameter (a) during compression and decompression; (b), selected 2D SAXS patterns of randomly layered superlattice consisting of In_2O_3 truncated nano-octahedra during compression and decompression; (c-e), structure models of the 2D close-packed layer: (c) a structure model corresponding to Stage

I, (d) a structure model of "ideal" planar packing position with maximum *a*, (e) a structure model corresponding to Stages II-IV.

While the WAXS data revealed no phase transition during the pressure variation, the SAXS of the randomly layered superlattice consisting of In_2O_3 truncated nano-octahedra exhibited intriguing behaviors. To analyze the SAXS patterns, we used the (11) reflection peak instead of the (10) to calculate the randomly layered superlattice unit cell parameter, denoted as "*a*". This choice was made because the (10) reflection peak is partially obscured by the beam stop (Fig. 3a,b) in addition to the aforementioned reason, which could lead to inaccurate peak fitting (*vide supra*). Fig. S6 displays selected 1D patterns of SAXS captured during compression and decompression. We fit the (11) peaks using Fityk software[64] across all collected patterns under various pressures, achieving the superlattice unit cell parameter, *a*. Fig. 4a illustrates the variation of "*a*" throughout the entire compressive and decompressive process, while Fig. 4b displays selected 2D patterns of SAXS during compression and decompression.

The compressive process can be categorized into three stages based on changes in *a*. Stage I extends from ambient pressure (0 GPa to 4.12 GPa), during which *a* rapidly decreased from $20.8\underline{6}$ nm to $20.1\underline{6}$ nm. Throughout this stage, the superlattice maintains its structure of closely packed layers, with no discernible translation of the octahedron within the layers (Fig. 4c). The decrease in *a* is attributed solely to the contraction of the ligands, as depicted in Fig. 5a. Stage II spans the pressure range from 4.61 GPa (Fig. S5j) to 8.43 GPa (Fig. S5o). During this stage, *a* slowly drops from $20.1\underline{4}$ nm to $20.1\underline{1}$ nm at 6.01 GPa, followed by a slow increase to $20.1\underline{4}$ nm at 8.43 GPa, with minor fluctuations.

This observed phenomenon can be attributed to the rising pressure, which causes the truncated nano-octahedra, encapsulated with organic ligands, to lose their capacity to retain their relative positions under the *p31m* symmetry. Consequently, the building blocks embark on a unique form of translation that is characteristic of their octahedral shape. As depicted in Fig. 4d, the commencement of this translation expands the distance between octahedron 1 and octahedron 2, while the angle between the two octahedra stays constant. This type of translation results in a larger cell parameter relative to the original unit cell of the superlattice. Simultaneously, the layer transitions from a hexagonally close-packed arrangement to a less densely packed structure. Despite the increasing parameter *a*, the relative positions of all reflections persist unchanged due to the constant angle of the randomly layered superlattice unit cell, while the *d*-spacings enlarge. Concurrently, the contacting length of the capped ligands continues to contract, consequently tending to reduce the superlattice cell parameter, *a* (Fig. 5a). During the outset of Stage II, the decrease in *a* continues, albeit at a considerably slower rate than Stage I, as the onset of the translation begins to counterbalance the ligand contraction (Fig. 4e, Fig. 5a). Midway through Stage II, the parameter-augmenting effect caused by the translation of octahedra gradually surpasses the parameter-reducing effect resulting from ligand contraction.[65] This sequence culminates in a decrease of *a* to its minimal value, followed by a fluctuating increase. By the closure of Stage II, the persistent increase in *a* signals that the influence of ligand contraction has become less significant compared to the effect of the octahedron translation. During Stage III, the translation of octahedra emerged as the primary factor influencing *a*, resulting in a rapid surge in *a*, from 9.01 GPa up to the peak pressure of 18.01 GPa. This observation marks the first instance of pressure-induced translation in self-assembled 2D superlattices comprising truncated nano-octahedra. The translation model, depicted in Fig. 4e, is unique to octahedra, further reinforcing the hexagonally close-packed structure. During decompression (Stage IV), *a* continued to rise steadily, reaching $21.7\underline{7}$ nm upon the completion of decompression. Compared with the initial *a* ($20.8\underline{6}$ nm) before pressure was applied, the post-pressure *a* value ($21.7\underline{7}$ nm) is approximately 0.9 nm larger, suggesting that the pressure change process is irreversible. In contrast to the compression process, during which *a* was influenced by both octahedron translation and ligand contraction, the steady increase of *a* during decompression suggests that the decreasing pressure primarily leads to the restoration of ligand length, with no associated octahedron translation. Consequently, the octahedron translation was triggered solely by increasing pressure and was accompanied by the irreversible disconnection of binding ligands. The theoretical maximum cell parameter, excluding the ligand, can be calculated as $a_{\max} = \sqrt{2}\, r_c = 21.5\underline{2}$ nm, assuming the vertex of one octahedron aligns with the vertex of another as illustrated in Fig. 4d. When the ligand length is considered (Fig. 5a), the maximum theoretical cell parameter, $\text{a̋}_{\max}$, should be $\text{a̋}_{\max} = a_{\max} + d_{\text{ligand}} = 21.5\underline{2} + 2.0\underline{5} = 23.5\underline{7}$ nm. This indicates that the octahedra didn't reach their theoretical maximum positions since $21.7\underline{7}$ nm < $23.5\underline{7}$ nm.

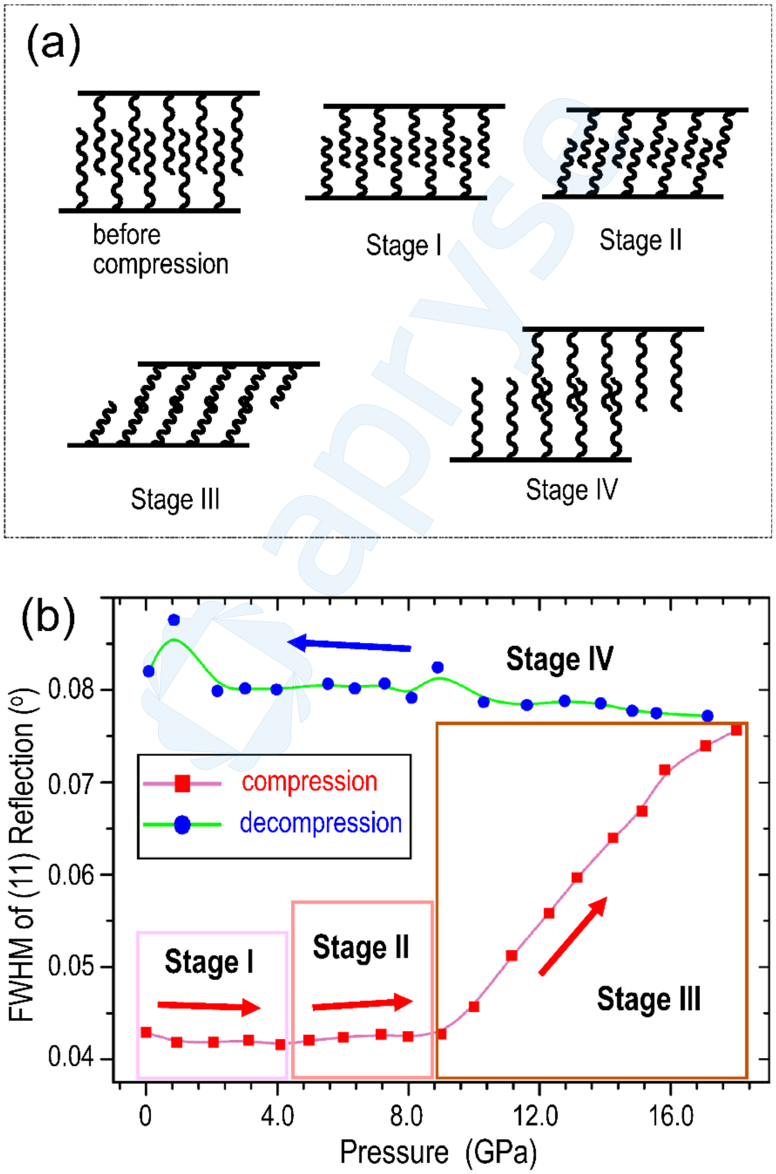

Fig. 5. Diffraction and ligand in randomly layered superlattice consisting of In_2O_3 truncated nano-octahedra. (a), illustration of ligand interaction in different stages; (b), the full width at half maximum (FWHM) of the SAXS (11) reflection peak as a function of pressure.

Pressure-Induced Crystallinity of Randomly Layered Superlattice

Fig. 5b illustrates the relationship between pressure and the full width at half maximum (FWHM) of the (11) reflection peak during both compressive and decompressive processes. The superlattice preserved its crystallinity during both Stages I and II, where ligand contraction was the primary driver of the cell parameter change. This caused the planar *p31m* symmetry to remain unchanged, hence exerting minimal impact on the degree of crystallinity. Conversely, during Stage III, the superlattice partially lost its ordered arrangements, as evidenced by the swift increase in the FWHM of the (11) reflection peak (Fig. 5b) from 9.01 GPa to 18.01 GPa. Two primary reasons can explain this change: 1) the extensive octahedron translation process during Stage III was not uniform across every layer or every point within the same layer, resulting in the displacement of octahedra from their ideal *p31m* symmetry positions (Fig. 4e); 2) unlike the ligand contraction process, ligands continued to bind each other during this stage, and the direction of octahedron movement was perpendicular to the ligands (Fig. 5a). As a result, octahedron translation was paired with the breaking of binding ligands, which likely led to layer fragmentation into smaller parts and subsequent peak broadening. Additionally, higher pressure might induce a sintering process,[54] leading to an increase in total entropy[66] by disrupting the *p31m* symmetry and causing irreversible phase transition (*vide infra*). In Stage IV, the FWHM continued to increase, albeit at a significantly slower rate, as pressure was released from 17.13 GPa to 0.08 GPa. As noted earlier, octahedron translation is irreversible during decompression. Hence, Stage IV solely involved ligand restoration, without any additional octahedron translation, irrespective of local positioning (at the end or center of the octahedron sides). This led to minimal variation in the superlattice's crystallinity during this stage. Essentially, the FWHM of the (11) reflection peak was utilized to further verify the behaviors of octahedron translation and ligand interaction during pressure variations. It's worth noting that an asymmetric diffraction spot emerged at the edge of the (11) reflection ring (Fig. 4b) at 13.15 GPa. This spot grew more intense as pressure rose to the peak value of 18.01 GPa and maintained its intensity during decompression until 11.62 GPa. This asymmetric diffraction spot is likely the result of a long-range ordered structure initiated by high pressure.

Conclusions

In this study, we synthesized In_2O_3 nano-octahedra, notable for their vertex truncation, and characterized their unique superlattice. Leveraging TEM observations, we determined the average circumradius of the octahedral building blocks to be 15.2 nm. Subsequently, we carried out synchrotron studies of WAXS and SAXS on the superlattice under various pressure conditions. The WAXS measurements confirmed the absence of phase transitions across the range of applied pressures, whereas SE imaging and SAXS data indicated that the superlattice is comprised of randomly distributed layers. Each layer adopts a lozenge shape, characterized by an obtuse angle of 120° in alignment with the wallpaper group *p31m*. Concurrently, the SAXS results disclosed an irreversible translation of octahedra within this randomly layered superlattice under pressure. The examination of the pressure-dependent superlattice cell parameter and the FWHM of the (11) reflection peak shed light on the differing influences of octahedron translation and ligand interaction across four distinct stages of compression and decompression. This investigation constitutes the first unveiling of pressure-induced translation in a randomly layered superstructure consisting of truncated nano-octahedron building blocks. The identified unique translation model, inherent to octahedra, further reinforces the evidence supporting a hexagonally close-packed superstructure.

Acknowledgments

This work was partially supported by the National Science Foundation (NSF) under grant DMR-1808383. X.C. and G.Z. are thankful for the financial support by the NSF under grant DMR-1905422. CHESS is supported by the NSF awards of DMR-1332208 and DMR-1829070. X.C. and L.Z. acknowledge the use of TEM facilities for the structural characterizations, at the Center for Functional Nanomaterials, which is a U.S. Department of Energy Office of Science User Facility, at Brookhaven National Laboratory under Contract No. DE-SC0012704. Preliminary TEM imaging work was supported by S3IP/ADL, the State University of New York at Binghamton, and CASM, Texas Tech University.

Supporting Information

The Supporting Information is available free of charge at xxx.

1. Experimental Section: chemicals, synthesis and self-assembly methods, high-pressure X-ray diffraction determination method, EM characterization method, and structural analysis method; 2. Supplemental Figures: the relationship between the distance d_t of two parallel facets and circumradius r_c in a perfect octahedron, TEM images of In_2O_3 truncated nano-octahedra dissolved from their superlattices, packing fraction calculation, simulated SAXS patterns with proposed unit cells and parameters of superlattices consisting of In_2O_3 truncated nano-octahedra, lattice parameters of $Im\overline{3}$ In_2O_3 unit cell received from Rietveld refinement of WAXS patterns during the compressive and decompressive processes, and selected 1D SAXS patterns of randomly layered superlattice consisting of In_2O_3 truncated nano-octahedra during compression and decompression; 3. References.

Corresponding Author

Jiye Fang - Department of Chemistry, Materials Science and Engineering Program, State University of New York at Binghamton, Binghamton, New York 13902, United States. orcid.org/0000-0003-3703-3204; Email: jfang@binghamton.edu

Authors

Shaojie Jiang, Materials Science and Engineering Program, State University of New York at Binghamton, Binghamton, New York 13902, United States. orcid.org/0000-0001-8692-0673

Xiaobo Chen, Materials Science and Engineering Program, State University of New York at Binghamton, Binghamton, New York 13902, United States. orcid.org/0000-0003-2943-2926

Xin Huang, Cornell High Energy Synchrotron Source, Cornell University, Ithaca, New York 14853, United States. orcid.org/0000-0001-5404-4437

Can Li, Department of Chemistry, State University of New York at Binghamton, Binghamton, New York 13902, United States. orcid.org/0000-0001-8894-5110

Zhongwu Wang, Cornell High Energy Synchrotron Source, Cornell University, Ithaca, New York 14853, United States. orcid.org/0000-0001-9742-5213

Bo Zhao, College of Arts & Sciences Microscopy, Texas Tech University, Lubbock, Texas 79409, United States. orcid.org/0000-0002-0813-3137

Lihua Zhang, Center for Functional Nanomaterials, Brookhaven National Laboratory, Upton, New York 11973, United States. orcid.org/0000-0003-3331-2345

Guangwen Zhou, Department of Mechanical Engineering, Materials Science and Engineering Program, State University of New York at Binghamton, Binghamton, New York 13902, United States. orcid.org/0000-0002-9243-293X

Notes

The authors declare no competing financial interest.

TOC

References:

1. Delerue, C.; Prins, P. T.; Vanmaekelbergh, D.; Hens, Z. Dielectric and Optical Properties of Superlattices of Epitaxially Connected Nanocrystals. *Phys. Rev. B: Condens. Matter* **2023,** *107* (24), 245413.

2. Urban, J. J.; Talapin, D. V.; Shevchenko, E. V.; Murray, C. B. Self-Assembly of PbTe Quantum Dots into Nanocrystal Superlattices and Glassy Films. *J. Am. Chem. Soc.* **2006,** *128* (10), 3248-3255.

3. Taleb, A.; Petit, C.; Pileni, M. P. Optical Properties of Self-Assembled 2D and 3D Superlattices of Silver Nanoparticles. *J. Phys. Chem. B* **1998,** *102* (12), 2214-2220.

4. Chang, C.-C.; Wu, H.-L.; Kuo, C.-H.; Huang, M. H. Hydrothermal Synthesis of Monodispersed Octahedral Gold Nanocrystals with Five Different Size Ranges and Their Self-Assembled Structures. *Chem. Mater.* **2008,** *20* (24), 7570-7574.

5. Voos, M. Some Properties of Semiconductor Superlattices. *Ann. des Telecommun.* **1988,** *43* (7), 357-364.

6. Dong, A.; Chen, J.; Oh, S. J.; Koh, W.-k.; Xiu, F.; Ye, X.; Ko, D.-K.; Wang, K. L.; Kagan, C. R.; Murray, C. B. Multiscale Periodic Assembly of Striped Nanocrystal Superlattice Films on a Liquid Surface. *Nano Lett.* **2011,** *11* (2), 841-846.

7. Tam, E.; Podsiadlo, P.; Shevchenko, E.; Ogletree, D. F.; Delplancke-Ogletree, M.-P.; Ashby, P. D. Mechanical Properties of Face-Centered Cubic Supercrystals of Nanocrystals. *Nano Lett.* **2010,** *10* (7), 2363-2367.

8. Yao, K. X.; Yin, X. M.; Wang, T. H.; Zeng, H. C. Synthesis, Self-Assembly, Disassembly, and Reassembly of Two Types of Cu_2O Nanocrystals Unifaceted with {001} or {110} Planes. *J. Am. Chem. Soc.* **2010,** *132* (17), 6131-6144.

9. Boles, M. A.; Engel, M.; Talapin, D. V. Self-Assembly of Colloidal Nanocrystals: From Intricate Structures to Functional Materials. *Chem. Rev.* **2016,** *116* (18), 11220-11289.

10. Collier, C. P.; Vossmeyer, T.; Heath, J. R. Nanocrystal Superlattices. *Annu. Rev. Phys. Chem.* **1998,** *49* (1), 371-404.

11. Huang, M. H.; Thoka, S. Formation of Supercrystals through Self-Assembly of Polyhedral Nanocrystals. *Nano Today* **2015,** *10* (1), 81-92.

12. Damasceno, P. F.; Engel, M.; Glotzer, S. C. Predictive Self-Assembly of Polyhedra into Complex Structures. *Science* **2012,** *337* (6093), 453-457.

13. Henzie, J.; Grünwald, M.; Widmer-Cooper, A.; Geissler, P. L.; Yang, P. Self-Assembly of Uniform Polyhedral Silver Nanocrystals into Densest Packings and Exotic Superlattices. *Nat. Mater.* **2012,** *11* (2), 131-137.

14. Lu, W.; Liu, Q.; Sun, Z.; He, J.; Ezeolu, C.; Fang, J. Super Crystal Structures of Octahedral c-In_2O_3 Nanocrystals. *J. Am. Chem. Soc.* **2008,** *130* (22), 6983-6991.

15. Zhuang, J.; Wu, H.; Yang, Y.; Cao, Y. C. Controlling Colloidal Superparticle Growth Through Solvophobic Interactions. *Angew. Chem. Int. Ed.* **2008,** *47* (12), 2208-2212.

16. Quan, Z.; Fang, J. Superlattices with Non-Spherical Building Blocks. *Nano Today* **2010,** *5* (5), 390-411.

17. Nagaoka, Y.; Tan, R.; Li, R.; Zhu, H.; Eggert, D.; Wu, Y. A.; Liu, Y.; Wang, Z.; Chen, O. Superstructures Generated from Truncated Tetrahedral Quantum Dots. *Nature* **2018,** *561* (7723), 378-382.

18. Ahniyaz, A.; Sakamoto, Y.; Bergstrom, L. Magnetic Field-Induced Assembly of Oriented Superlattices from Maghemite Nanocubes. *Proc. Natl. Acad. Sci.* **2007,** *104* (45), 17570-17574.

19. Zhang, J.; Kumbhar, A.; He, J.; Das, N. C.; Yang, K.; Wang, J.-Q.; Wang, H.; Stokes, K. L.; Fang, J. Simple Cubic Super Crystals Containing PbTe Nanocubes and Their Core−Shell Building Blocks. *J. Am. Chem. Soc.* **2008,** *130* (45), 15203-15209.

20. Demortiere, A.; Launois, P.; Goubet, N.; Albouy, P. A.; Petit, C. Shape-Controlled Platinum Nanocubes and Their Assembly into Two-Dimensional and Three-Dimensional Superlattices. *J. Phys. Chem. B* **2008,** *112* (46), 14583-14592.

21. Shen, X. S.; Wang, G. Z.; Hong, X.; Zhu, W. Simple-Cubic Microcubes Assembled by Palladium Nanocubes. *CrystEngComm* **2009,** *11* (5), 753-755.

22. Zhang, J.; Luo, Z.; Quan, Z.; Wang, Y.; Kumbhar, A.; Smilgies, D.-M.; Fang, J. Low Packing Density Self-Assembled Superstructure of Octahedral Pt_3Ni Nanocrystals. *Nano Lett.* **2011,** *11* (7), 2912-2918.

23. Zhu, Z.; Meng, H.; Liu, W.; Liu, X.; Gong, J.; Qiu, X.; Jiang, L.; Wang, D.; Tang, Z. Superstructures and SERS Properties of Gold Nanocrystals with Different Shapes. *Angew. Chem. Int. Ed.* **2011,** *50* (7), 1593-1596.

24. Gong, J.; Newman, R. S.; Engel, M.; Zhao, M.; Bian, F.; Glotzer, S. C.; Tang, Z. Shape-Dependent Ordering of Gold Nanocrystals into Large-Scale Superlattices. *Nat. Commun.* **2017,** *8* (1), 14038.

25. Li, R.; Zhang, J.; Tan, R.; Gerdes, F.; Luo, Z.; Xu, H.; Hollingsworth, J. A.; Klinke, C.; Chen, O.; Wang, Z. Competing Interactions between Various Entropic Forces toward Assembly of Pt_3Ni Octahedra into a Body-Centered Cubic Superlattice. *Nano Lett.* **2016,** *16* (4), 2792-2799.

26. Minkowski, H. Dichteste Gitterförmige Lagerung Kongruenter Körper. *Nachr. Ges. Wiss. Gottingen, Math.-Phys. Kl.* **1904,** *1904* ( ), 311-355.

27. Lee, Y. H.; Lay, C. L.; Shi, W.; Lee, H. K.; Yang, Y.; Li, S.; Ling, X. Y. Creating Two Self-Assembly Micro-Environments to Achieve Supercrystals with Dual Structures using Polyhedral Nanoparticles. *Nat. Commun.* **2018,** *9* (1), 2769.

28. Avci, C.; Imaz, I.; Carné-Sánchez, A.; Pariente, J. A.; Tasios, N.; Pérez-Carvajal, J.; Alonso, M. I.; Blanco, A.; Dijkstra, M.; López, C.; Maspoch, D. Self-Assembly of Polyhedral Metal-Organic Framework Particles into Three-Dimensional Ordered Superstructures. *Nat. Chem.* **2018,** *10* (1), 78-84.

29. Smith, D. K.; Goodfellow, B.; Smilgies, D.-M.; Korgel, B. A. Self-Assembled Simple Hexagonal AB_2 Binary Nanocrystal Superlattices: SEM, GISAXS, and Defects. *J. Am. Chem. Soc.* **2009,** *131* (9), 3281-3290.

30. Chu, X.; Abelson, A.; Qian, C.; Igouchkine, O.; Field, E.; Ma, K.-L.; Law, M.; Moule, A. J. Atomic Lattice Resolved Electron Tomography of a 3D Self-Assembled Mesocrystal. *Adv. Funct. Mater.* **2023,** *33* (22), 2301026.

31. Nasilowski, M.; Mahler, B.; Lhuillier, E.; Ithurria, S.; Dubertret, B. Two-Dimensional Colloidal Nanocrystals. *Chem. Rev.* **2016,** *116* (18), 10934-10982.

32. Saikia, B. K.; Boruah, R. K.; Gogoi, P. K. A X-ray Diffraction Analysis on Graphene Layers of Assam Coal. *J. Chem. Sci.* **2009,** *121* (1), 103-106.

33. Stobinski, L.; Lesiak, B.; Malolepszy, A.; Mazurkiewicz, M.; Mierzwa, B.; Zemek, J.; Jiricek, P.; Bieloshapka, I. Graphene Oxide and Reduced Graphene Oxide Studied by the XRD, TEM and Electron Spectroscopy Methods. *J. Electron. Spectrosc. Relat. Phenom.* **2014,** *195*, 145-154.

34. Arguelles, A.; Leoni, M.; Blanco, J. A.; Marcos, C. Semi-Ordered Crystalline Structure of the Santa Olalla Vermiculite Inferred from X-ray Powder Diffraction. *Am. Miner.* **2010,** *95* (1), 126-134.

35. Grangeon, S.; Claret, F.; Linard, Y.; Chiabergea, C. X-ray Diffraction: A Powerful Tool to Probe and Understand the Structure of Nanocrystalline Calcium Silicate Hydrates. *Acta Cryst.* **2013,** *69*, 465-473.

36. Roth, W. J.; Gil, B.; Makowski, W.; Marszalek, B.; Eliasova, P. Layer Like Porous Materials with Hierarchical Structure. *Chem. Soc. Rev.* **2016,** *45* (12), 3400-3438.

37. Ebina, Y.; Akatsuka, K.; Fukuda, K.; Sasaki, T. Synthesis and In Situ X-ray Diffraction Characterization of Two-Dimensional Perovskite-Type Oxide Colloids with a Controlled Molecular Thickness. *Chem. Mat.* **2012,** *24* (21), 4201-4208.

38. Sakharov, B. A.; Lanson, B., Chapter 2.3 - X-ray Identification of Mixed-Layer Structures: Modelling of Diffraction Effects. In *Developments in Clay Science*, Bergaya, F.; Lagaly, G., Eds. Elsevier: 2013; Vol. 5, pp 51-135.

39. Yang, D.; Frindt, R. F. Powder X-ray Diffraction of Two-Dimensional Materials. *J. Appl. Phys.* **1996,** *79* (5), 2376-2385.

40. Liu, H.; Yang, X.; Wang, K.; Wang, Y.; Wu, M.; Zuo, X.; Yang, W.; Zou, B. Pressure-Induced Multidimensional Assembly and Sintering of $CuInS_2$ Nanoparticles into Lamellar Nanosheets with Band Gap Narrowing. *ACS Appl. Nano Mater.* **2020,** *3* (3), 2438-2446.

41. Laue, M. Cross-Lattice Spectra. *Z. Krist* **1932,** *82*, 127-141.

42. Warren, B. E. X-Ray Diffraction in Random Layer Lattices. *Phys. Rev.* **1941,** *59* (9), 693-698.

43. Hendricks, S.; Teller, E. X-ray Interference in Partially Ordered Layer Lattices. *J. Chem. Phys.* **1942,** *10* (3), 147-167.

44. Wilson, A. X-ray Diffraction by Random Layers: Ideal Line Profiles and Determination of Structure Amplitudes from Observed Line Profiles. *Acta Crystallogr.* **1949,** *2* (4), 245-251.

45. Brindley, G. W.; Mering, J. Diffractions des Rayons X par les Structures en Couches Desordonnees. *Acta Crystallogr.* **1951,** *4* (5), 441-447.

46. Plançon, A. The Calculation of Intensities Diffracted by a Partially Oriented Powder with a Layer Structure. *J. Appl. Crystallogr.* **1980,** *13* (6), 524-528.

47. Treacy, M. M. J.; Newsam, J. M.; Deem, M. W. A General Recursion Method For Calculating Diffracted Intensities From Crystals Containing Planar Faults. *P. Roy. Soc.-Math. Phys. Sci.* **1991,** *433* (1889), 499-520.

48. Leoni, M.; Gualtieri, A. F.; Roveri, N. Simultaneous Refinement of Structure and Microstructure of Layered Materials. *J. Appl. Crystallogr.* **2004,** *37*, 166-173.

49. Casas-Cabanas, M.; Rodríguez-Carvajal, J.; Palacín, M. R., FAULTS, A New Program for Refinement of Powder Diffraction Patterns from Layered Structures. In *Ninth European Powder Diffraction Conference*, Oldenbourg Wissenschaftsverlag: München, 2006; pp 243-248.

50. Ufer, K.; Kleeberg, R.; Bergmann, J.; Dohrmann, R. Rietveld Refinement of Disordered Illite-Smectite Mixed-Layer Structures by a Recursive Algorithm. I: One-Dimensional Patterns. *Clays Clay Miner.* **2012,** *60* (5), 507-534.

51. Ufer, K.; Kleeberg, R.; Bergmann, J.; Dohrmann, R. Rietveld Refinement of Disordered Illite-Smectite Mixed-Layer Structures by a Recursive Algorithm. II: Powder-Pattern Refinement and Quantitative Phase Analysis. *Clays Clay Miner.* **2012,** *60* (5), 535-552.

52. Bai, F.; Bian, K.; Huang, X.; Wang, Z.; Fan, H. Pressure Induced Nanoparticle Phase Behavior, Property, and Applications. *Chem. Rev.* **2019,** *119* (12), 7673-7717.

53. Zhao, D.; Wang, M.; Xiao, G.; Zou, B. Thinking about the Development of High-Pressure Experimental Chemistry. *J. Phys. Chem. Lett.* **2020,** *11* (17), 7297-7306.

54. Meng, L.; Vu, T. V.; Criscenti, L. J.; Ho, T. A.; Qin, Y.; Fan, H. Theoretical and Experimental Advances in High-Pressure Behaviors of Nanoparticles. *Chem. Rev.* **2023,** *123* (16), 10206-10257.

55. Marezio, M. Refinement of the Crystal Structure of In_2O_3 at Two Wavelengths. *Acta Crystallogr.* **1966,** *20* (6), 723-728.

56. Lee, Y. H.; Shi, W.; Lee, H. K.; Jiang, R.; Phang, I. Y.; Cui, Y.; Isa, L.; Yang, Y.; Wang, J.; Li, S.; Ling, X. Y. Nanoscale Surface Chemistry Directs The Tunable Assembly of Silver Octahedra into Three Two-Dimensional Plasmonic Superlattices. *Nat. Commun.* **2015,** *6* (1), 6990.

57. Allen, A. J., Section 5.8.3.1.1. Guinier Approximation. In *Volume H: Powder diffraction of "International Tables for Crystallography"* 1st ed.; Gilmore, C. J.; Kaduk, J. A.; Schenk, H., Eds., 2019; p 683.

58. Guinier, A.; Fournet, G. *Small-Angle Scattering of X-Rays*. John Wiley & Sons, Inc., New York, 1955.

59. Lin, Y.-C.; Chen, C.-Y.; Chen, H.-L.; Hashimoto, T.; Chen, S.-A.; Li, Y.-C. Hierarchical Self-Assembly of Nanoparticles in Polymer Matrix and the Nature of the Interparticle Interaction. *J. Chem. Phys.* **2015,** *142* (21), 214905.

60. Reichhelm, A.; Haubold, D.; Eychmüller, A. Ligand Versatility in Supercrystal Formation. *Adv. Funct. Mater.* **2017,** *27* (39), 1700361.

61. Wang, Z.; Wen, X.-D.; Hoffmann, R.; Son, J. S.; Li, R.; Fang, C.-C.; Smilgies, D.-M.; Hyeon, T. Reconstructing A Solid-Solid Phase Transformation Pathway in CdSe Nanosheets with Associated Soft Ligands. *Proc. Natl. Acad. Sci.* **2010,** *107* (40), 17119-17124.

62. García-Domene, B.; Sans, J. A.; Gomis, O.; Manjón, F. J.; Ortiz, H. M.; Errandonea, D.; Santamaría-Pérez, D.; Martínez-García, D.; Vilaplana, R.; Pereira, A. L. J.; Morales-García, A.; Rodríguez-Hernández, P.; Muñoz, A.; Popescu, C.; Segura, A. Pbca-Type In_2O_3: The High-Pressure Post-Corundum Phase at Room Temperature. *J. Phys. Chem. C* **2014,** *118* (35), 20545-20552.

63. Qi, J.; Liu, J. F.; He, Y.; Chen, W.; Wang, C. Compression Behavior and Phase Transition of Cubic In_2O_3 Nanocrystals. *J. Appl. Phys.* **2011,** *109* (6), 063520.

64. Wojdyr, M. Fityk: A General-Purpose Peak Fitting Program. *J. Appl. Crystallogr.* **2010,** *43* (5 Part 1), 1126-1128.

65. Xiao, T.; Nagaoka, Y.; Wang, X.; Jiang, T.; LaMontagne, D.; Zhang, Q.; Cao, C.; Diao, X.; Qiu, J.; Lu, Y.; Wang, Z.; Cao, Y. C. Nanocrystals with Metastable High-Pressure Phases under Ambient Conditions. *Science* **2022,** *377* (6608), 870-874.

66. Zhang, J.; Zhu, J.; Li, R.; Fang, J.; Wang, Z. Entropy-Driven Pt_3Co Nanocube Assembles and Thermally Mediated Electrical Conductivity with Anisotropic Variation of the Rhombohedral Superlattice. *Nano Lett.* **2017,** *17* (1), 362-367.